

Synchrotron Intensity Gradient Revealing Magnetic Fields in Galaxy Clusters

Yue Hu^{1,2,*}, C. Stuardi^{3,4}, A. Lazarian^{2,*}, G. Brunetti⁴, A. Bonafede^{3,4}, and Ka Wai Ho^{2,5}

¹Department of Physics, University of Wisconsin-Madison, Madison, WI 53706, USA

²Department of Astronomy, University of Wisconsin-Madison, Madison, WI 53706, USA

³Dipartimento di Fisica e Astronomia, Università di Bologna, via Gobetti 93/2, I-40129 Bologna, Italy

⁴INAF - Istituto di Radioastronomia di Bologna, Via Gobetti 101, I-40129 Bologna, Italy

⁵Theoretical Division, Los Alamos National Laboratory, Los Alamos, NM 87545, USA

*e-mail: yue.hu@wisc.edu, alazarian@facstaff.wisc.edu

ABSTRACT

Magnetic fields and their dynamical interplay with matter in galaxy clusters contribute to the physical properties and evolution of the intracluster medium. However, the current understanding of the origin and properties of cluster magnetic fields is still limited by observational challenges. In this article, we map the magnetic fields at hundreds-kpc scales of five clusters RXC J1314.4 -2515, Abell 2345, Abell 3376, MCXC J0352.4 -7401, and El Gordo using the synchrotron intensity gradient technique in conjunction with high-resolution radio observations from the Jansky Very Large Array (JVLA) and the Karoo Array Telescope (MeerKAT). We demonstrate that the magnetic field orientation of radio relics derived from synchrotron intensity gradient is in agreement with that obtained with synchrotron polarization. Most importantly, the synchrotron intensity gradient is not limited by Faraday depolarization in the cluster central regions and allows us to map magnetic fields in the radio halos of RXC J1314.4 -2515 and El Gordo. We find that magnetic fields in radio halos exhibit a preferential direction along the major merger axis and show turbulent structures at higher angular resolution. The results are consistent with expectations from numerical simulations, which predict turbulent magnetic fields in cluster mergers that are stirred and amplified by matter motions.

Introduction

Magnetic fields are a ubiquitous aspect of the cosmos¹⁻³, and the largest-scale cosmic magnetic fields observed to date are found in galaxy clusters⁴⁻⁷. These magnetic fields are a fundamental part of cosmic magnetogenesis, either arising from the turbulent amplification of seed fields or being injected by active galactic nuclei and galaxies^{8,9}. They are critical to maintaining energy balance within the intracluster medium (ICM) through heat conduction^{10,11}, coupling cosmic rays (CRs) to the intracluster gas¹²⁻¹⁴, and generating synchrotron radiation by gyrating CR electrons¹⁵. Despite the crucial importance, the origin of magnetic fields in ICM remains the grand challenge problem. To check the existing theoretical predictions that the magnetic field can be amplified during the galaxy mergers¹⁶⁻¹⁹, a comprehensive understanding of magnetic field topology in galaxy clusters is imperative.

The study of magnetic fields in galaxy clusters is typically based on observing polarized radio emissions from background or embedded radio galaxies and diffuse synchrotron sources. The Faraday Rotation Measure (RM) of a polarized source, obtained from the rotation of its polarization angle with wavelength, reveals the line-of-sight (LOS) magnetic field weighted by thermal electron density. An RM grid constructed using many background polarized sources provides a valuable probe of the cluster's magnetic field structure^{20,21}. This approach established that the magnetic fields of the cluster were turbulent and tangled on spatial scales between 5 and 500 kpc²². However, these findings are limited by the number of detected background polarized sources, and the uncertainties related to the RM grid interpretation are still not well defined²³. The plane-of-the-sky (POS) magnetic field orientation is revealed by direct detection of linearly polarized emission^{1,24}, but, as we discussed further, this way of probing the magnetic field fails for most of the galactic cluster volume.

Polarized diffuse synchrotron emissions, particularly from radio relics and halos, allow the study of magnetic fields within selected regions of galaxy clusters. For instance, strongly polarized radio relics (with polarization fraction up to 60%) that are typically located at the cluster's periphery can be explored this way^{6,19,25}. However, depolarization effects, such as Faraday depolarization caused by thermal electrons and turbulent magnetic fields along the LOS, as well as beam depolarization due to a randomized magnetic field distribution in the POS, prevent this type of studies for most extended regions of clusters, i.e., galactic halos^{26,27}. Thus, so far, no polarization mapping of magnetic fields in radio halos has been carried out. This is one of the main challenges faced by the next-generation radio facilities, such as the Square Kilometre Array (SKA)^{28,29}.

Based on a comprehensive understanding of the pervasive MHD turbulence in the ICM, the refs.³⁰⁻³² introduced synchrotron

intensity gradient (SIG) as a way to map the magnetic fields. The fast turbulent reconnection in MHD turbulence leads to the mixing of magnetized plasma perpendicular to the direction of the local magnetic field. This results in anisotropic structures of turbulent velocity, magnetic field, and synchrotron radiation elongating along the magnetic field^{33,34}, as confirmed by numerical simulations^{35–38} and in situ measurements in the solar wind^{39–41}. As a result, the direction of SIG determines the magnetic field, as was proven by comparing the magnetic fields traced by SIG and synchrotron polarization for the Milky Way magnetic fields³⁰. This analysis was further substantiated through numerical simulations that replicated the turbulent conditions within the Milky Way³⁰. Nevertheless, it is crucial to recognize that the nature of turbulence within galaxy clusters is distinctly different from the turbulence observed within the Milky Way⁴². Therefore, so far there has been only one attempt to apply SIG for magnetic field mapping in the relaxed cluster Perseus³². The application assumed the Alfvén scale, i.e., the scale at which magnetic fields become dynamically important⁴³, is observationally resolved. Based on the current study of turbulence and magnetic field strength in the ICM, the Alfvén scale is constrained from 1 to 60 kpc (see methods, subsection "SIG: theoretical consideration"). However, our numerical simulations (see methods, subsection "SIG: numerical testing") demonstrated that resolving the Alfvén scale is not essential for SIG. We showed that at scales larger than the Alfvén scale, magnetic fields passively follow the motion of the large-scale flow, with SIG aligned perpendicular to the magnetic field, similar to the case when the Alfvén scale is resolved (see methods, subsection "SIG: theoretical consideration"). This understanding underlines our confident application of SIG to the ICM.

Here we apply SIG to five disturbed galaxy clusters (RXC J1314.4-2515, Abell 2345, Abell 3376, MCXC J0352.4 - 7401, and El Gordo), which are of particular interest in terms of magnetic field amplification and the acceleration of cosmic rays by magnetized turbulence^{15,44}, using high-resolution radio observations obtained with the Jansky Very Large Array (JVLA)^{22,25} and the MeerKAT array⁴⁵. Our choice is motivated by the fact that magnetic fields in Abell 3376's and El Gordo's relics have already been studied by polarization^{46,47}, while the fields in the relics of RXC J1314.4-2515 and Abell 2345 was also recently mapped^{22,25}. Thus, these four clusters provide a valuable test bed for applying SIG. Encouraged by the consistency of the SIG results with observational and numerical testing, we use SIG to map the magnetic fields in the MCXC J0352.4-7401 cluster⁴⁵ and we present the magnetic field measurements in RXC J1314.4-2515 and El Gordo radio halos, revealing the structure of magnetic fields on the largest scales ever measured.

Results

Magnetic field morphology in RXC J1314.4 - 2515, Abell 2345, Abell 3376, MCXC J0352.4 - 7401, and El Gordo:

We follow the SIG³² adapted to clusters as discussed in methods, subsection "SIG: practical implementation" to map Plane of Sky (POS) magnetic fields in galaxy clusters RXC J1314.4-2515^{25,45}, Abell 2345²², Abell 3376⁴⁵, MCXC J0352.4 - 7401⁴⁵, and El Gordo⁴⁵. We define the Alignment Measure (AM) to quantify the alignment of the SIG and the polarization measurements: $AM = 2(\cos^2 \theta_r - \frac{1}{2})$, where θ_r is the relative angle between the POS magnetic field inferred from two methods. $AM = 1$ corresponds to a perfect parallel alignment, while $AM = -1$ represents a perpendicular alignment. The values of the AM are illustrated by chromatically superimposing the values onto the magnetic field vectors as inferred from polarization measurements and are shown in Figs. 1 and 2.

The detection of polarized synchrotron emission in radio relics in the peripheral regions of RXC J1314.4 - 2515 and Abell 2345 has been achieved through JVLA observation at a frequency range of 1-2 GHz^{22,25}. The resolution of the polarization signal, represented by the full width and half maximum (FWHM) of the Gaussian beam, is around 25" (or 120 kpc) for RXC J1314.4 - 2515 and around 30.5" (or 110 kpc) for Abell 2345. For RXC J1314.4 - 2515, SIG is calculated per pixel (beam resolution about 7.6" or 30 kpc) and averaged to FWHM about 25", which is similar to that of polarization signal. As shown in Figs. 1 and 3, the magnetic fields inferred from SIG and polarization are found to be in agreement (overall AM about 0.70, with a standard deviation of the mean around 0.01), aligned with the elongated intensity relics along the south-north direction. The measured AM is a bit lower compared to its AM obtained for SIG in Milky Way³⁰. We attribute this to the higher signal-to-noise and the smaller Faraday rotation effects in the Milky Way case.

SIG and polarization are sensitive to variations of magnetic field orientation with beam size. As shown in Fig. 8, AM decreases for a large beam. In addition, unlike SIG, polarization is sensitive to Faraday rotation and Faraday depolarization. As a result, we do expect to see differences between the polarization and SIs. The systematic difference between the two measures carries important information that sheds light on the difference in the physical mechanisms of the processes that reveal magnetic field direction, and this difference can be explored in future studies to get deeper insight into the physics of ICM.

Similarly, in Abell 2345, we obtain AM around 0.6 (see Fig. 2). The misalignment between the SIG and polarization in the south tail of Abell 2345-E can be attributed to the potential uncertainties in both measurements (as detailed in the Supplementary Information). In particular, we noticed that the misalignment is associated with a point source. These sources induce synchrotron intensity gradients that are not associated with magnetic fields. The removal of the point source increases the correspondence between polarization and SIG increases. On the other hand, intensity jumps at shock fronts may induce deviation in the SIG from that of the underlying magnetic field. However, as we discuss in the Supplementary Information, the

contribution of the shock fronts becomes marginal in the process of the sub-block averaging method adopted in SIG. For the relics of Abell 2345 the polarization resolution corresponds to FWHM about $30.5''$, which is higher than that of SIG, which potentially also affects the AM. Nevertheless, our study confirms the overall consistency between the directions the polarization and SIG revealed. This finding strengthens the rationale for using this technique in mapping magnetic fields in galaxy clusters where polarization has not been reported.

Figs. 4, 5, and 6 present the magnetic field measurement of the merging clusters Abell 3376, MXCX J0352.4-7401, and El Gordo using the SIG. These clusters have different redshifts (z approximately 0.87 for El Gordo, 0.127 for MXCX J0352.4-7401, and 0.046 for Abell 3376). The SIG measurements are in agreement with earlier partial polarization observations in Abell 3376's double relics⁴⁶ and El Gordo's west relic⁴⁷. The magnetic fields associated with radio galaxy jets and bent by ICM in Abell 3376 have also been observed in the SIG measurement⁴⁸. These earlier studies only covered limited portions of the relics with detected polarization signals, but the SIG measurements cover the entire structure and provide complete magnetic field maps. In addition, we present the SIG-mapped magnetic field for the detected relics in MCXC J0352.4-7401. Future high-resolution synchrotron intensity observations will enable SIG to map magnetic fields at smaller scales.

Measurement of polarized synchrotron emission in radio halos is challenging due to the strong Faraday depolarization effect. SIG, however, offers a unique solution to this problem as it is insensitive to depolarization. As a result, SIG opens an avenue for studying the magnetic field of radio halos. For example, in RXC J1314.4-2515 and El Gordo, polarization is detected only in the double relics²⁵ and the west relic⁴⁷, respectively. However, SIG provides a complete picture of the magnetic fields in the entire cluster, including halos (see Figs. 1 and 6). Due to the beam and LOS averaging, the gradient signals caused by small-scale fluctuations are averaged out in the central radio halo. SIG, however, remains sensitive to the large-scale component of the magnetic field (see methods, subsection "SIG: theoretical consideration"). At low resolution, the magnetic field in RXC J1314.4-2515 (see Fig. 1 in the Supplementary Information) is preferentially aligned along the merger axis, whereas on top of this behavior, vortex-like start appearing at higher resolution (see Fig. 1), yet limited to effective 120 kpc resolution. The maps clearly show the transition between radio relics and halos, which are associated with shock waves where the magnetic field is compressed in the direction perpendicular to the merger axis (see Figs. 4 and 5 in the Supplementary Information).

Discussion

The reported magnetic field structure testifies the magnetic field amplification during galactic mergers. It is in line with previous RM grid measurements²² and MHD simulations that predicted magnetic fields evolve with cluster dynamics¹⁶⁻¹⁹ (see Fig. 7 for an illustration). The fields are stretched/stirred and further amplified by large-scale bulk flows along the merger axis. On the other hand, the presence of large-scale magnetic fields suggests that the magnetic field amplification through turbulent dynamo is rather inefficient at its non-linear stage, in which less than 10% of turbulent kinetic energy is transferred to magnetic field energy^{44,49}. Thus, for stationary turbulence, it would take around ten of the longest eddy turnover times for the magnetic field to reach equipartition with turbulence. Since the merging of clusters did not last for such a long time, the more prominent magnetic field structures are formed through the large-scale stretching caused by the flows resulting from the merger. We anticipate that there are more magnetic field stochasticity on the small scale.

Our results open perspectives to map magnetic fields in clusters and large-scale structures and allow for the comparison between numerical expectations of merging clusters and observations. SIG's ability to trace the galaxy clusters' magnetic fields is confirmed by (a) MHD simulations presented in Fig. 8, (b) the correspondence of SIG with polarization measurements in radio relics (see Figs. 1 and 2), as well as (c) the correspondence of the SIG-traced halo magnetic field structure to those numerically predicted in the refs.¹⁶⁻¹⁹. Being insensitive to the Faraday depolarization, SIG can be applied to many clusters with diffuse radio emission, which is especially timely in view of the coming SKA and the Low-Frequency Array (LOFAR) observations. It opens a unique way of using radio data for the regions where depolarization masks and distorts the polarized signal. The prospects of SIG get more exciting in view of recent LOFAR observations that discovered synchrotron radiation on large scales (several Mpc), on the outskirts of the cluster or between massive cluster pairs⁵⁰⁻⁵². As soon as high signal-to-noise images of this very large-scale synchrotron emission become available, SIG will also enable us to map these largest-scale magnetic fields and study their statistic properties (see Fig. 6 in the Supplementary Information for an example of the statistical analysis via the structure-function). This will provide constraints on the theories of magneto-genesis of magnetic field and their role within large-scale structures of Universe evolution.

Methods

SIG: theoretical consideration

SIG introduced in ref.³⁰⁻³² is extended in this paper for super-Alfvénic turbulence present in the ICM. In the super-Alfvénic regime (i.e., $M_A > 1$), turbulent motions at the injection scale are hydrodynamic, and the kinetic energy of the turbulence follows an isotropic Kolmogorov cascade ($v_l \approx l^{1/3}$, where v_l is the velocity of the turbulence at scale l). However, at smaller scales, the backreaction of the magnetic field becomes stronger and the turbulence becomes anisotropic on the Alfvén scale $l_A = LM_A^{-3}$, where L is the injection scale⁵³. The typical Alfvén scale in galaxy clusters can be calculated as follows⁴³:

$$l_A \approx 100 \left(\frac{B}{\mu\text{G}} \right)^3 \left(\frac{L}{300 \text{ kpc}} \right) \left(\frac{v_L}{10^3 \text{ km s}^{-1}} \right)^{-3} \left(\frac{n_e}{10^{-3} \text{ cm}^{-3}} \right)^{-\frac{3}{2}} \text{pc}, \quad (1)$$

where B is the magnetic field strength, L is the injection scale of turbulence, and n_e is the electron number density. Based on typical values of B (0.5 - 2.0 μG), L (300 - 600 kpc), v_L (100 - 300 km s^{-1}), and n_e (10^{-3} cm^{-3}) from literature^{25,54-59}, the Alfvén scale l_A ranges from approximately 1 - 60 kpc. Note that quoted values of the physical quantities are typically measured for cluster cores. In the edges of the cluster, these values may be different.

At scales smaller than l_A , the anisotropic MHD turbulence causes the turbulent eddies to elongate along the magnetic field, resulting in a gradient perpendicular to the field. At scales larger than l_A , the large-scale gas flows can still regulate the dynamically unimportant magnetic field in the ICM, causing the field to follow or elongate along large-scale structures, as shown in Fig. 8. Therefore, the actual number of l_A is not important for using SIG to map the magnetic field, because the gradients are perpendicular to the magnetic field in both cases.

SIG: comparison with polarization

SIG and synchrotron polarization are based on different physical effects to reveal the magnetic field. While synchrotron polarization emerges from the magnetic fields' effects on relativistic electrons, SIG is grounded in the interaction between magnetic fields and conducting fluid. Notably, measurements obtained from both methods are subject to the effects of LOS averaging. Given the expected scenario where the LOS integration length for cluster halos surpasses the scale of magnetic field entanglement, turbulence-induced fluctuations are not anticipated to manifest a preferential direction, instead accumulating through a process akin to a random walk. These turbulence-driven fluctuations play a pivotal role in decreasing the synchrotron polarization fraction, known as Faraday depolarization. However, SIG is immune to the depolarization effect, maintaining its reliability in tracing the magnetic fields in super-Alfvénic radio halos. As illustrated in Fig. 8, the alignment between SIG and magnetic fields remains statistically stable, even when the LOS integration length increases. On the other side, polarization is sensitive not only to the value of the magnetic field strength that aligns parallel to the LOS but also to the density of thermal electrons within the environment. Given that the orientation of magnetic fields within galaxy clusters is subject to changes along the LOS, there is a possibility for differences between contributions to SIG and those to polarization.

A factor that can induce misalignment in observational applications is the beam size. This effect can be illustrated by considering a particular example of a very large beam, which covers the full field of view of the observation. Such a beam results in a constant intensity map and the corresponding gradient vanishes, but polarization still can give one magnetic field orientation for this large beam. This beam effect, therefore, reduces the alignment as shown in the right panel of Fig. 8.

SIG: practical implementation

In this study, SIG serves as the primary tool for analysis. The intensity gradient calculated from the synchrotron intensity map ($I(x, y)$) allows for mapping the orientation of magnetic fields. This is achieved through a pixelized gradient map $\psi(x, y)$ as follows:

$$\begin{aligned} \nabla_x I(x, y) &= I(x+1, y) - I(x, y), \\ \nabla_y I(x, y) &= I(x, y+1) - I(x, y), \\ \psi(x, y) &= \tan^{-1} \left(\frac{\nabla_y I(x, y)}{\nabla_x I(x, y)} \right), \end{aligned} \quad (2)$$

here, $\nabla_x I(x, y)$ and $\nabla_y I(x, y)$ represent the x and y components of the gradient, respectively. Gradients are blanked out if their corresponding intensity value is less than 3σ noise level.

The gradient map $\psi(x, y)$ is further processed through the sub-block averaging method⁶⁰. This method involves taking all gradient orientations within a sub-block of interest and applying Gaussian fitting to the corresponding histogram. The peak value of the Gaussian distribution represents the statistically most probable gradient orientation within that sub-block. The averaging step ensures that the resulting gradient direction incorporates turbulence's statistical properties. The processed gradient map is denoted as $\psi_s(x, y)$, and its uncertainty is related to the sub-block size. A larger sub-block size guarantees a

sufficient amount of data for statistical fitting, leading to lower uncertainty. Typically, gradients are averaged over 20×20 -pixel sub-blocks, as this size has been determined through previous numerical and observational studies to guarantee sufficient statistics for extracting turbulence's properties⁶¹. To address the boundary effect in cases where the number of data points at the edge of an intensity structure may be less than 20×20 pixels, a minimum of 10×10 pixels is established for averaging.

The averaging procedure for each sub-block is independent. However, this is not the case for actual magnetic field lines, necessitating a correlation of the averaged gradient with that of its neighboring. This can be mathematically handled by performing smoothing on the pseudo-Stokes parameters (Q_g and U_g), which are defined as:

$$\begin{aligned} Q_g(x, y) &= I(x, y) \cos(2\psi_s(x, y)), \\ U_g(x, y) &= I(x, y) \sin(2\psi_s(x, y)), \\ \psi_g(x, y) &= \frac{1}{2} \tan^{-1}\left(\frac{U_g}{Q_g}\right), \end{aligned} \quad (3)$$

where ψ_g is the pseudo polarization angle. Similar to the Planck polarization, $\psi_B = \psi_g + \frac{\pi}{2}$ gives the POS magnetic field orientation. The weighted intensity ensures that (i) Q_g and U_g follow a Gaussian distribution, which facilitates the smoothing of the pseudo-Stokes parameters using a Gaussian filter. The FWHM of the Gaussian filter is equal to the sub-block size. (ii) The magnetic fields mapped by SIG are intensity-weighted, which is also the case for the magnetic field inferred from synchrotron polarization weighted by the polarized intensity.

SIG: uncertainty

The uncertainty in SIG is mainly due to systematic errors in radio images and the SIG algorithm itself. We calculated SIG's uncertainty by considering error propagation and blanked out the pixels in which the uncertainty is larger than 30 degrees. We presented the uncertainty maps in Supplementary Figs. 2 and 3 and listed the median value of the uncertainty for each cluster in Tab. 2.

SIG: numerical testing

A numerical test is presented for illustration purposes. In accordance with the method described in the ref.³⁰, we utilize several 3D MHD simulations of turbulence to synthesize synchrotron emission maps, including the synchrotron intensity $I_s(x, y)$, Stokes parameters $Q_s(x, y)$ and $U_s(x, y)$, and polarization angle $\psi(x, y)$. Each simulation box is divided into 512^3 cells, with a turbulence injection scale of approximately 256 cells. The calculation of these maps is based on the following equations:

$$\begin{aligned} I_s &= \int n_{e,r} (B_x^2 + B_y^2) B_\perp^\gamma dz, \\ Q_s &= \int -n_{e,r} (B_x^2 - B_y^2) B_\perp^\gamma dz, \\ U_s &= \int -n_{e,r} (2B_x B_y) B_\perp^\gamma dz, \\ \psi &= \frac{1}{2} \tan^{-1}\left(\frac{U}{Q}\right), \end{aligned} \quad (4)$$

where $B_\perp = \sqrt{B_x^2 + B_y^2}$ is the magnetic field component perpendicular to the LOS, with B_x and B_y being the x and y components, respectively, and $n_{e,r}$ is the density of relativistic electrons. In consideration of the fact that the anisotropy of synchrotron emission is insensitive to the spectral index of the electron energy distribution⁶², a homogeneous and isotropic distribution with spectral index $\alpha = 3$ is adopted, yielding an index of $\gamma = \frac{\alpha-3}{4}$.

An example is shown in the left panel of Fig. 8. The super-Alfvénic condition of $M_A \approx 3.2$ leads to a turbulence length scale of $l_A \approx 8$ cells. The magnetic field orientation inferred from SIG globally agrees with that derived from polarization (with an agreement measure of $AM \approx 0.81$). The AM values for other simulations are listed in Tab. 1, which demonstrates correspondence of the magnetic field orientation mapped by polarization and SIG.

Observational data: intensity of synchrotron emission

The synchrotron emission images used in this work are produced with JVLA and MeerKAT observations. The summary of the data set is presented in Tab. 2.

RXC J1314.4-2515: polarization images with similar resolution thanks to the images released by the MeerKAT Galaxy Cluster Legacy Survey Data Release 1 (<https://archive-gw-1.kat.ac.za/public/repository/10.48479/7epd-w356/index.html>). The high resolution 1.28 GHz image from which we derived the SIG measurements (see Fig. 1) has a beam size of $7.3'' \times 7.6''$ corresponding to a spatial resolution of about 30 kpc at $z = 0.247$. The RMS noise of this

image is $5 \mu\text{Jy}/\text{beam}$. Instead, a low-resolution SIG image was obtained from the same JVLA dataset from which we derived polarization (see Fig. 1 in the Supplementary Information). This total intensity image at 3GHz has a resolution of $17'' \times 17''$, corresponding to 66 kpc around, and an RMS noise of $13 \mu\text{Jy}/\text{beam}$. This image is the same as the one presented by the ref.²⁵ but smoothed with a circular beam size.

Abell 2345: The resolution beam of the 1.5 GHz JVLA total intensity map in Fig. 2 is $19'' \times 19''$, corresponding to a spatial resolution of 58 kpc at $z = 0.179$. With respect to the image presented by ref.²² this has been smoothed to obtain a circular beam size. The RMS noise is $80 \mu\text{Jy}/\text{beam}$.

Abell 3376: The resolution beam of the 1.28 GHz MeerKAT total intensity images of this cluster shown in Fig. 4 is $7.4'' \times 7.6''$, corresponding to a spatial resolution of approximately 7 kpc at $z = 0.046$. The RMS noise is $3.1 \mu\text{Jy}/\text{beam}$.

MCXC J0352.4 - 7401 (Abell 3186): The total intensity 1.28 GHz MeerKAT images of this cluster shown in Fig. 5 have a resolution beam of $6.9'' \times 7.1''$. This corresponds to a spatial resolution of approximately 16 kpc at $z = 0.127$. The RMS noise is $2.6 \mu\text{Jy}/\text{beam}$.

El Gordo: The resolution beam of the total intensity 1.28 GHz MeerKAT image of El Gordo shown in Fig. 6 is $7.1'' \times 7.1''$, corresponding to a physical resolution of approximately 55 kpc at $z = 0.87$. The RMS noise is $1.5 \mu\text{Jy}/\text{beam}$.

Observational data: polarization measurement

We use the synchrotron polarization measurements obtained from JVLA observations^{22,25}. We only report here the main characteristics of these observations while we refer to the original works for a detailed explanation of the data analysis. The magnetic field orientation is defined as $\chi_B = \chi_0 + \frac{\pi}{2}$, inferred from the intrinsic polarization angle χ_0 at the source obtained with the Rotation Measure synthesis technique⁶³. This is intended to correct the measured Faraday rotation to represent the magnetic-field orientation at the relic.

Nevertheless, radio images can be affected by polarization leakage between Stokes parameters due to instrumental effects. The leakage from Stokes I to Q and U was estimated at less than 2 %^{22,25}. Since relics are highly polarized, the leakage should have a marginal effect on the polarization angle estimates. The uncertainty of mapping magnetic fields with polarization can also arise from the adopted model of the distribution of thermal and relativistic electrons within the relics⁶⁴. The uncertainty of the order 10° can serve as an estimate for the misalignment of polarization and SIG vectors, which corresponds to the reported AM variation of ± 0.2 .

The magnetic field orientation images of the RXC J1314.4-2515 galaxy cluster were obtained from a 1-2 GHz JVLA observation (with a central frequency of 1.5 GHz and resolution beam of $25''$) while a 2-4 GHz JVLA observation (central frequency of 3 GHz and resolution beam of $30.5''$) was used for Abell 2345. The polarization images are not smoothed further but re-gridded to match that of the SIG-measured magnetic field orientation spatially. Polarization images are already masked to show only pixels detected with a corresponding Gaussian significance level greater than 5σ , as explained in refs.^{22,25}.

Tables

M_A	2.4	2.9	3.2	5.2	7.8
AM	0.92	0.93	0.81	0.88	0.92

Table 1. Summary of global mean AM values in different Alfvén Mach number M_A conditions. The uncertainty of AM calculated from the standard deviation of the mean is around 0.01 - 0.02.

Cluster	Beam resolution (SIG)	$\langle \sigma_{\psi_g} \rangle$	Frequency	Polarization data (resolution)
RXC J1314.4-2515 ⁴⁵	30 kpc (120 kpc)	7.80°	1.28 GHz	JVLA 3 GHz (120 kpc) ²⁵
Abell 2345 ²²	58 kpc (180 kpc)	E: 5.79° , W: 3.83°	1.5 GHz	JVLA 1.5 GHz (110 kpc) ²²
Abell 3376 ⁴⁵	7 kpc (22 kpc)	E: 6.60° , W: 7.82°	1.28 GHz	-
MCXC J0352.4 - 7401 ⁴⁵	16 kpc (62 kpc)	E: 7.44° , W: 7.52°	1.28 GHz	-
El Gordo ⁴⁵	55 kpc (400 kpc)	7.41°	1.28 GHz	-

Table 2. Summary of data sets used in this work. $\langle \sigma_{\psi_g} \rangle$ is the median value of the SIG's uncertainty over the region of interest.

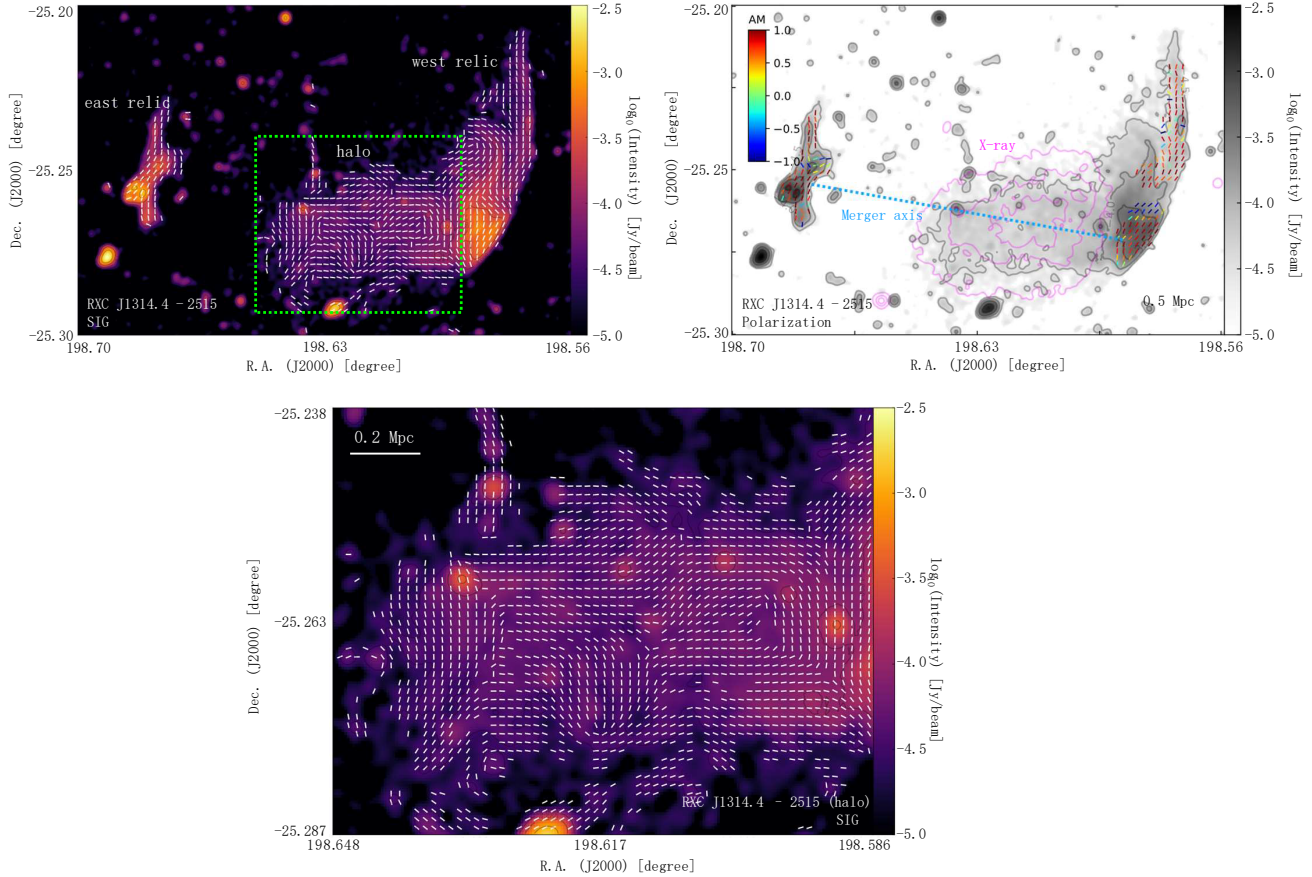


Figure 1. The magnetic field orientation of the RXC J1314.4 - 2515 galaxy cluster. Top: The differences and similarities of the magnetic fields measured by the two techniques (SIG and polarization) are presented. On the top left, the morphology of the magnetic fields is revealed through the SIG (FWHM around $25''$ or 120 kpc). On the top right, the magnetic field morphology is revealed through JVLA synchrotron polarization at 3 GHz (FWHM approximately $25''$). Each magnetic field segment represents the SIG (or polarization) averaged for 6×6 pixels for visualization purposes. The colors of the polarization segments represent the AM of the SIG and polarization. The magnetic field is overlaid on the higher resolution synchrotron emission image from the MeerKAT survey⁴⁵ at 1.28 GHz (FWHM around $7.6''$ or 30 kpc). The pink contours represent X-ray emission measured by the XMM-Newton and the dotted line indicates the expected merger axis determined by radio images. The merger axis defined by X-ray emission's elongation is studied in the Supplementary Information. Bottom: A zoom-in view of the magnetic field in RXC J1314.4 - 2515's halo, indicated by the green box in the top panel, is provided.

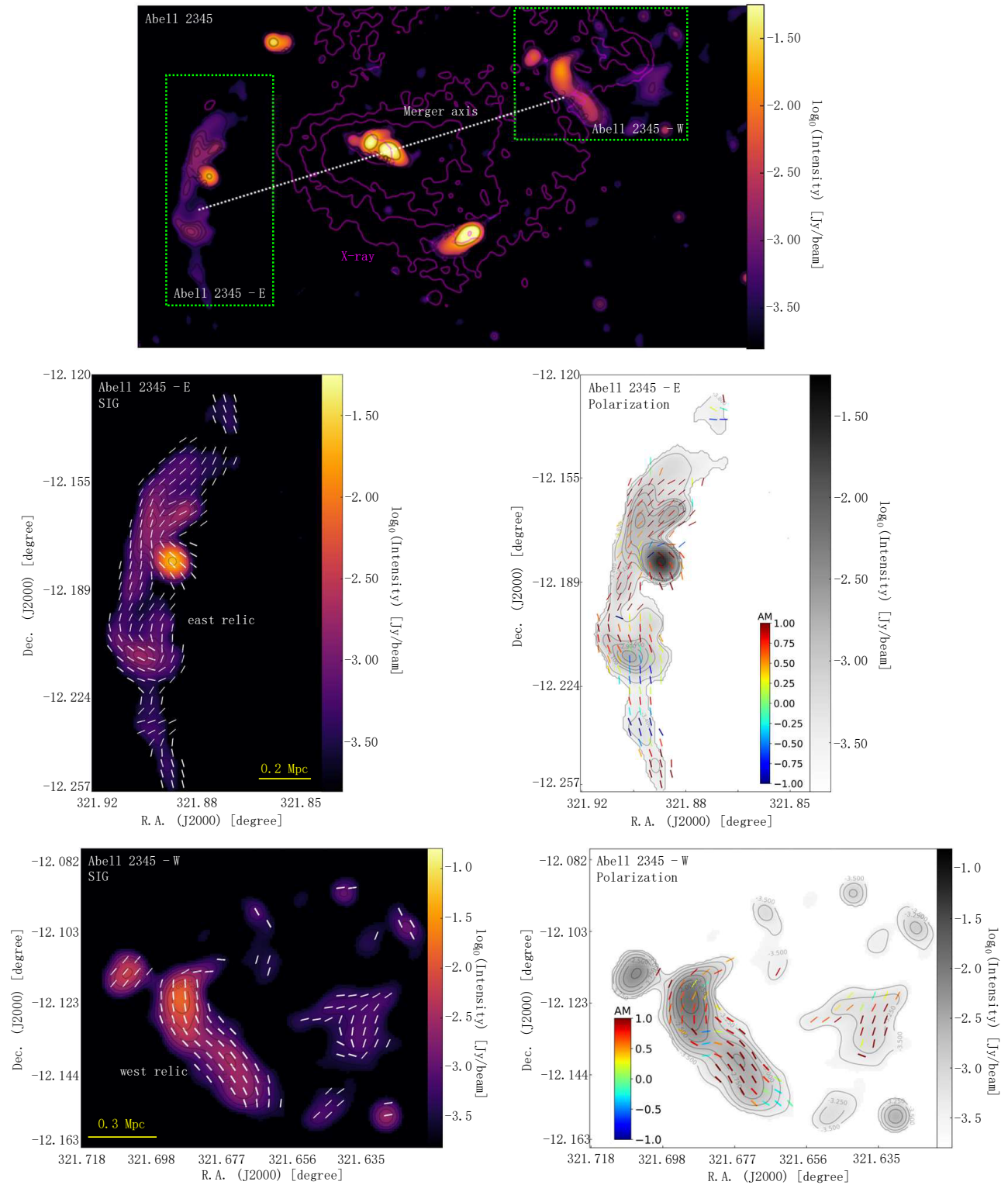


Figure 2. The magnetic field orientation of the Abell 2345 galaxy cluster. Top: Synchrotron emission image of the Abell 2345 cluster observed with the JVLA at 1.5 GHz. The pink contours represent X-ray emission measured by the XMM-Newton and the dotted line indicates the expected merger axis. Bottom: same as Fig. 1, but for the Abell 2345 cluster's subregion E (bottom left) and W (bottom right), indicated by the green boxes in the top panel. The magnetic field inferred from the synchrotron polarization and background emission image is from the JVLA observation at 1.5 GHz (FWHM approximately $30.5''$ or 110 kpc). The resolution of the SIG is approximately $50''$ (or 180 kpc).

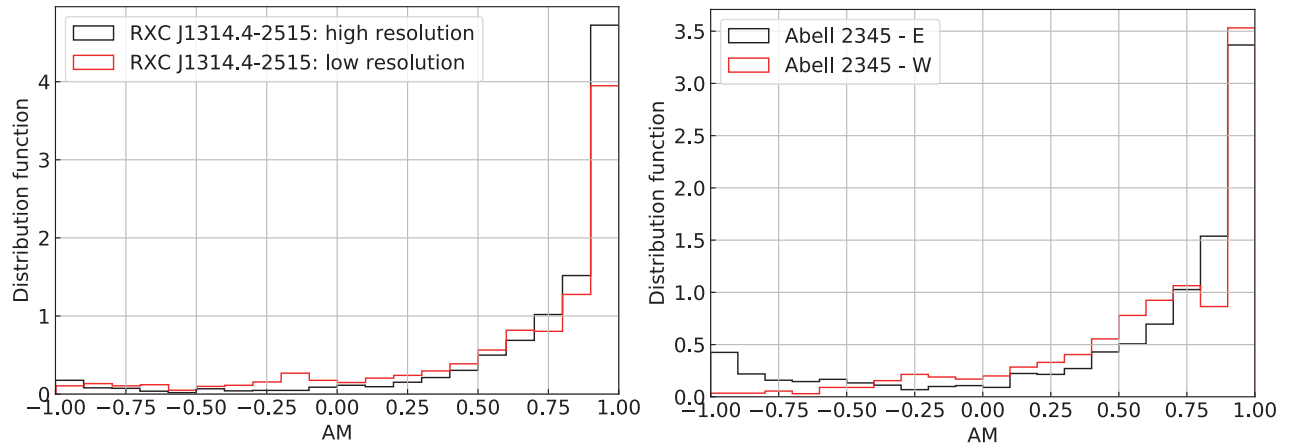


Figure 3. Histograms of AM (between the SIG and polarization) towards RXC J1314.4-2515 (left) and Abell 2345 (right). The maxima at AM = 1 suggests an excellent alignment of magnetic fields revealed by the two methods.

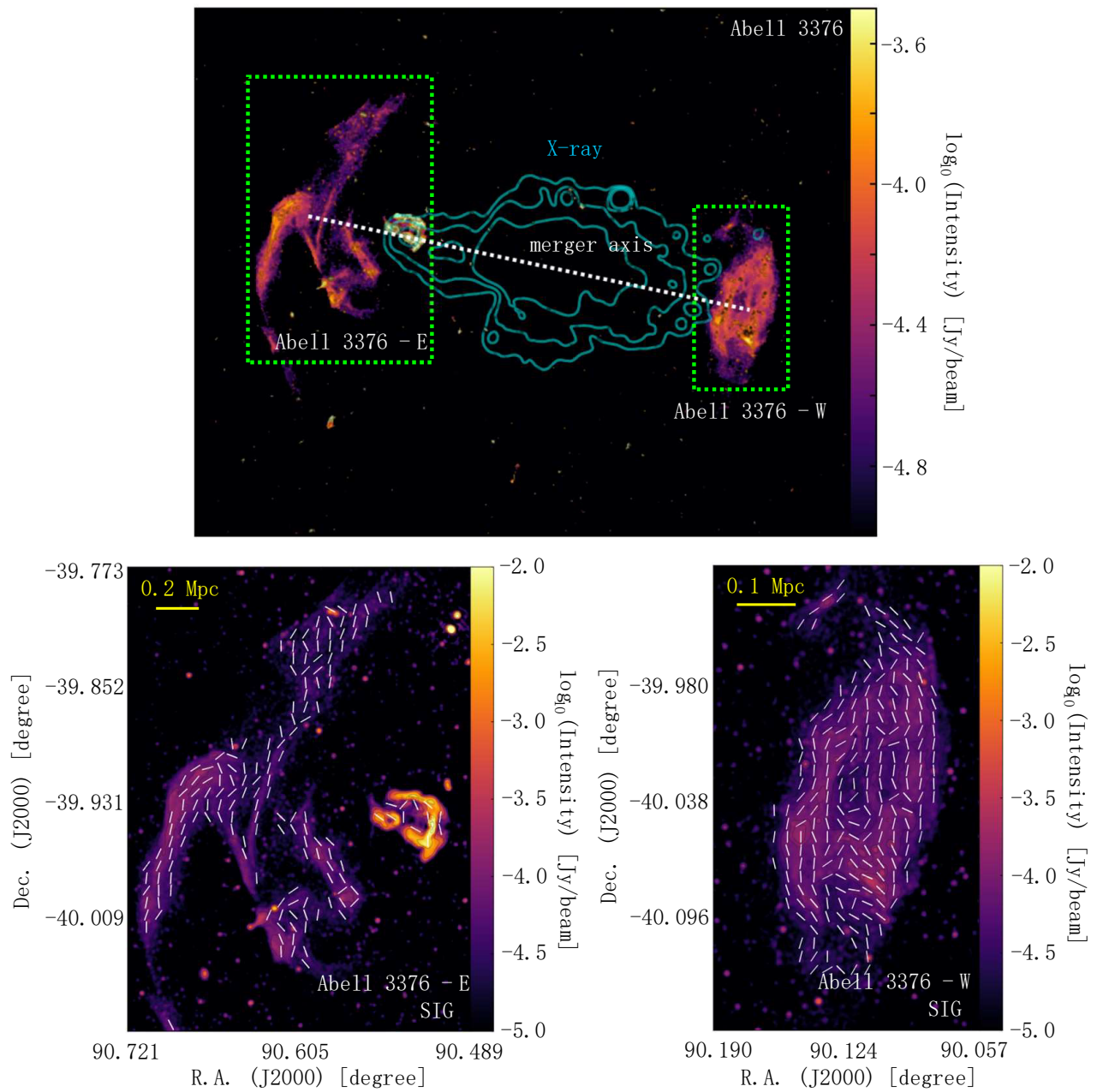


Figure 4. The magnetic field orientation of the Abell 3376 galaxy cluster. Top: overall synchrotron emission intensity map from MeerKAT observation at 1.28 GHz (FWHM approximately $7''$) of the Abell 3376 cluster. The cyan contours represent X-ray emission obtained from the XMM-Newton archival observations⁶⁵ and the dotted line indicates the expected merger axis. Bottom: The magnetic field orientation (FWHM approximately $24''$ corresponding to a physical scale of 22 kpc), represented by white segments, in Abell 3376's relics (indicated by the green boxes in the top panel).

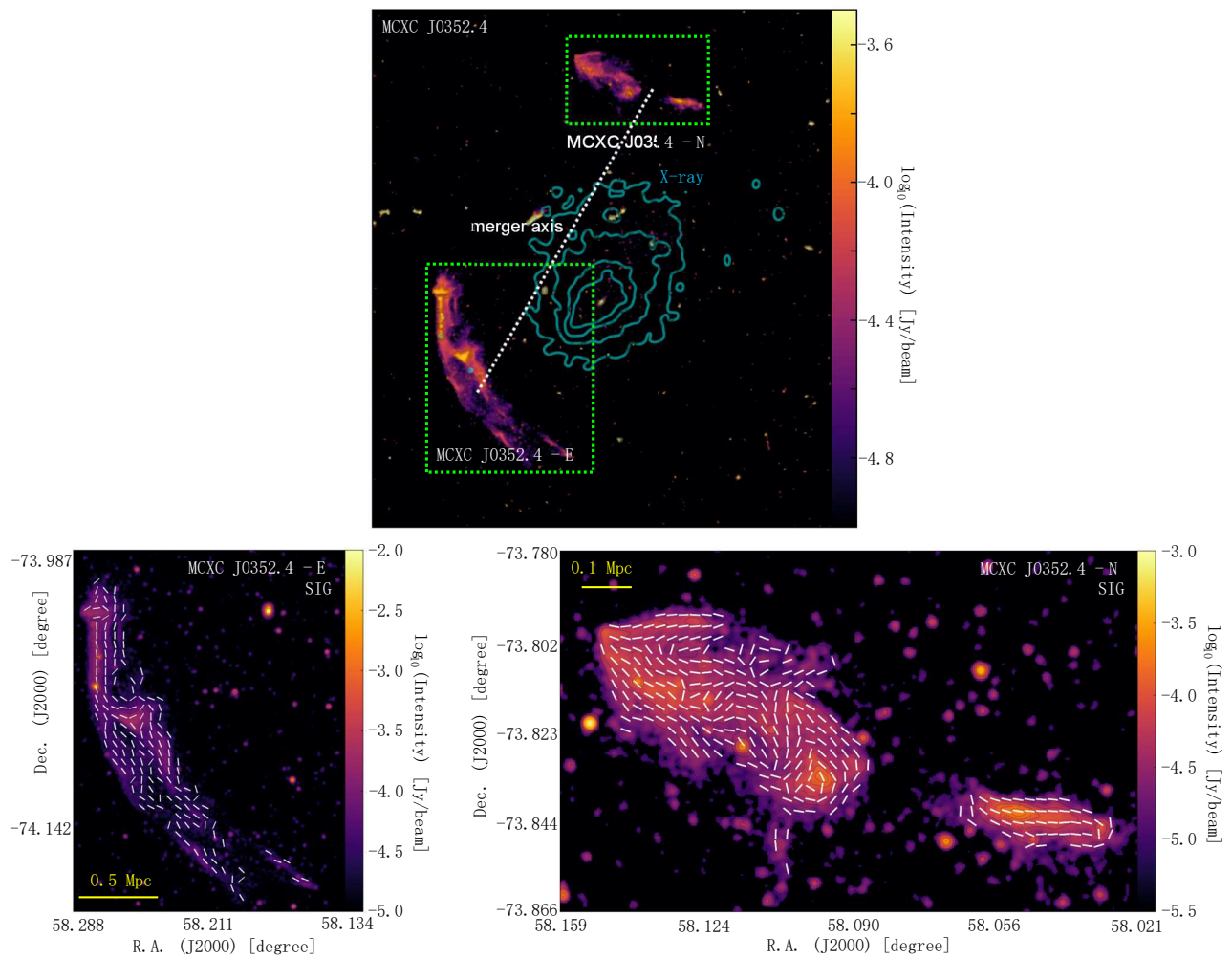


Figure 5. The magnetic field orientation of the MCXC J0352.4 - 7401 cluster⁶⁶. The magnetic field orientation (white segments), superimposed on the synchrotron emission intensity map from MeerKAT observation at 1.28 GHz (FWHM approximately $7''$), has resolution FWHM approximately $24''$ corresponding to physical scales of 62 kpc respectively).

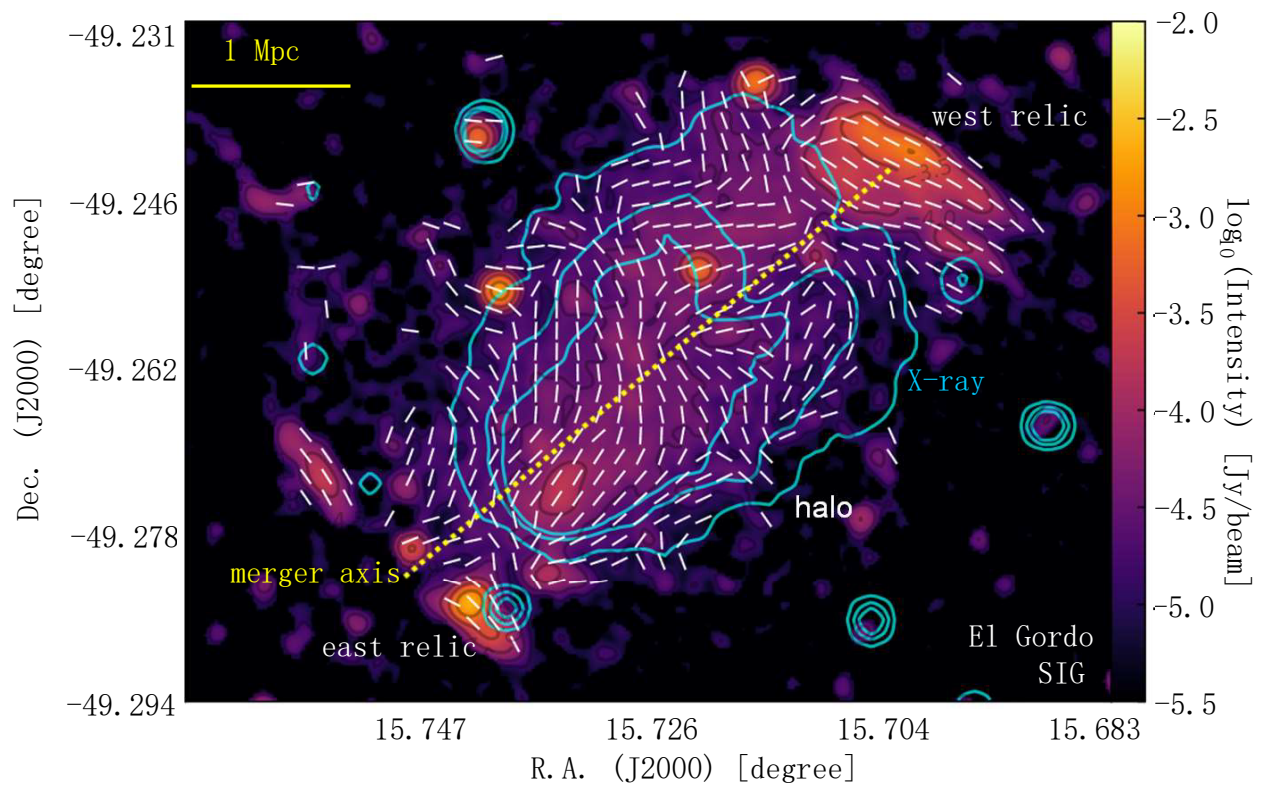


Figure 6. The magnetic field orientation of the El Gordo cluster. The background emission image is from MeerKAT observation at 1.28 GHz (FWHM approximately $7''$). The SIG measurement has a resolution of FWHM approximately $24''$ (or 400 kpc). Each white segment represents the SIG averaged for 6×6 pixels for visualization purposes. The blue contours represent the X-ray emission obtained from the Chandra archival observations⁶⁷ and the dotted line indicates the expected merger axis.

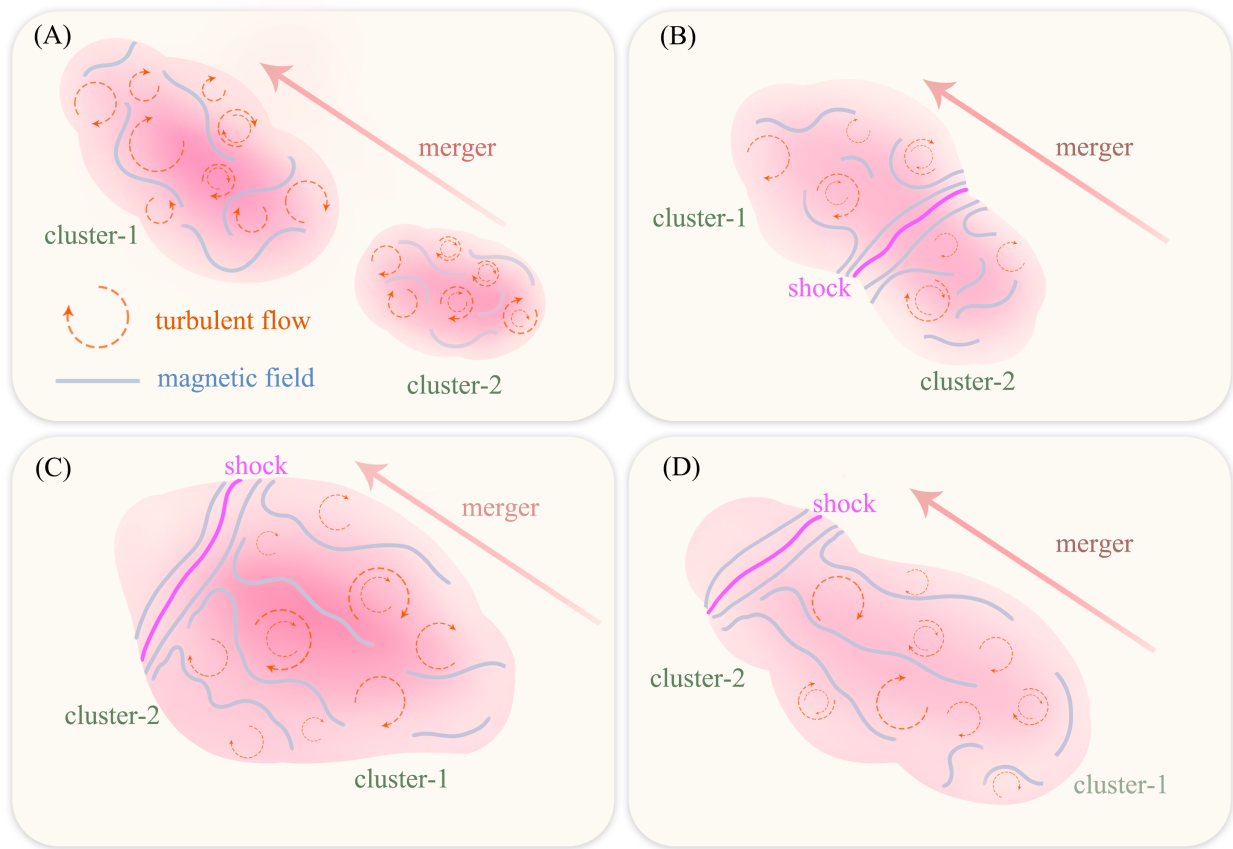


Figure 7. Cartoon illustration of magnetic field evolution in cluster merger. In the merging of two turbulent clusters (panel A): cluster-1 and cluster-2, the magnetic field is draped and amplified at the merger (advancing) shock in the first phase (panel B), then the field is stretched along the merger axis (panel C), and finally it is further amplified by turbulence generated in the cluster merger (panel D).

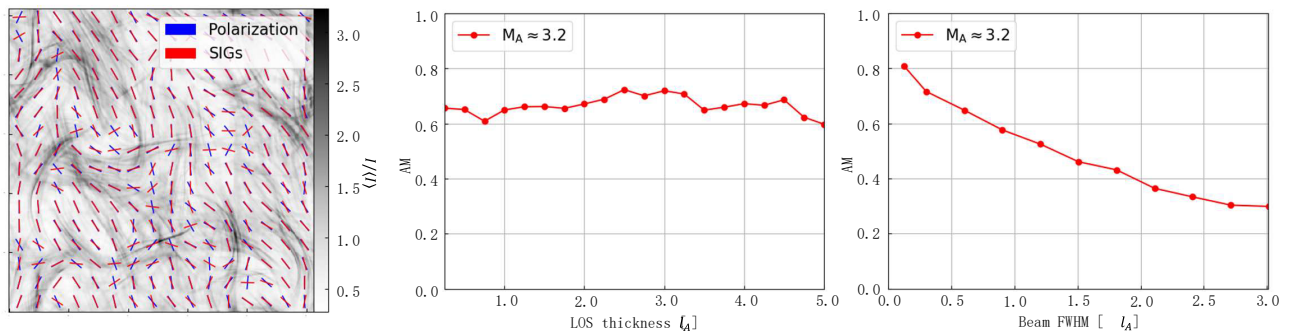


Figure 8. Numerical test of SIG. Left: comparison of the magnetic field orientation inferred from SIG (red segment) and polarization (blue segment). Middle and right: AM of magnetic fields inferred from SIG and polarization as a function of the cluster's LOS thickness (middle) and the beam size (right). Polarization is smoothed to match the resolution of SIG after averaging.

Data availability

Source data supporting the SIG plots and other findings presented in this paper are accessible from the MeerKAT Galaxy Cluster Legacy Survey Data Release 1: <https://archive-gw-1.kat.ac.za/public/repository/10.48479/7epd-w356/index.html> and JVLA data archive: <https://data.nrao.edu/portal/#/>. The datasets generated and analyzed during the current study are available from the corresponding author upon request.

Code availability

The simulations of MHD turbulence were conducted with the code MHDFlows, which can be downloaded from: <https://github.com/MHDFlows/MHDFlows.jl>. The analysis of the simulation data can be done with any science program language (e.g., Julia) according to the formulas provided explicitly in the manuscript. The SIG code supporting the findings of this study is available from the corresponding authors upon request. We have chosen not to publicly share the code in order to protect proprietary algorithms and maintain compliance with licensing agreements that restrict open distribution. We are committed to fostering scientific collaboration and are happy to provide the code to interested researchers for the purpose of replicating or building upon our findings.

References

1. Carilli, C. L. & Taylor, G. B. Cluster Magnetic Fields. *Annu. Rev. Astron. Astrophys.* **40**, 319–348 (2002).
2. Crutcher, R. M. Magnetic Fields in Molecular Clouds. *Annu. Rev. Astron. Astrophys.* **50**, 29–63 (2012).
3. Beck, R. Magnetic fields in spiral galaxies. *The Astron. Astrophys. Rev.* **24**, 4 (2015).
4. Ferrari, C., Govoni, F., Schindler, S., Bykov, A. M. & Rephaeli, Y. Observations of Extended Radio Emission in Clusters. *Space Sci. Rev.* **134**, 93–118 (2008).
5. Feretti, L., Giovannini, G., Govoni, F. & Murgia, M. Clusters of galaxies: observational properties of the diffuse radio emission. *The Astron. Astrophys. Rev.* **20**, 54 (2012).
6. van Weeren, R. J. *et al.* Diffuse Radio Emission from Galaxy Clusters. *Space Sci. Rev.* **215**, 16 (2019).
7. Botteon, A. *et al.* Magnetic fields and relativistic electrons fill entire galaxy cluster. *Sci. Adv.* **8**, eabq7623 (2022).
8. Grasso, D. & Rubinstein, H. R. Magnetic fields in the early Universe. *Phys. Reports* **348**, 163–266 (2001).
9. Subramanian, K. The origin, evolution and signatures of primordial magnetic fields. *Reports on Prog. Phys.* **79**, 076901 (2016).
10. McNamara, B. R. & Nulsen, P. E. J. Heating Hot Atmospheres with Active Galactic Nuclei. *Annu. Rev. Astron. & Astrophys.* **45**, 117–175 (2007).
11. Rephaeli, Y., Nevalainen, J., Ohashi, T. & Bykov, A. M. Nonthermal Phenomena in Clusters of Galaxies. *Space Sci. Rev.* **134**, 71–92 (2008).
12. Völk, H. J., Aharonian, F. A. & Breitschwerdt, D. The Nonthermal Energy Content and Gamma-Ray Emission of Starburst Galaxies and Clusters of Galaxies. *Space Sci. Rev.* **75**, 279–297 (1996).
13. Drake, J. F. *et al.* Whistler-regulated Magnetohydrodynamics: Transport Equations for Electron Thermal Conduction in the High- β Intracluster Medium of Galaxy Clusters. *ApJ* **923**, 245 (2021).
14. Berlok, T., Quataert, E., Pessah, M. E. & Pfrommer, C. Suppressed heat conductivity in the intracluster medium: implications for the magneto-thermal instability. *MNRAS* **504**, 3435–3454 (2021).
15. Brunetti, G. & Jones, T. W. Cosmic Rays in Galaxy Clusters and Their Nonthermal Emission. *Int. J. Mod. Phys. D* **23**, 1430007–98 (2014).
16. Roettiger, K., Stone, J. M. & Burns, J. O. Magnetic Field Evolution in Merging Clusters of Galaxies. *ApJ* **518**, 594–602 (1999).
17. Takizawa, M. N-Body + Magnetohydrodynamical Simulations of Merging Clusters of Galaxies: Characteristic Magnetic Field Structures Generated by Bulk Flow Motion. *ApJ* **687**, 951–958 (2008).
18. Vazza, F., Brunetti, G., Brügggen, M. & Bonafede, A. Resolved magnetic dynamo action in the simulated intracluster medium. *MNRAS* **474**, 1672–1687 (2018).
19. Donnert, J., Vazza, F., Brügggen, M. & ZuHone, J. Magnetic Field Amplification in Galaxy Clusters and Its Simulation. *Space Sci. Rev.* **214**, 122 (2018).

20. Murgia, M. *et al.* Magnetic fields and Faraday rotation in clusters of galaxies. *Astron. & Astrophys.* **424**, 429–446 (2004).
21. Bonafede, A. *et al.* The Coma cluster magnetic field from Faraday rotation measures. *Astron. & Astrophys.* **513**, A30 (2010).
22. Stuardi, C. *et al.* The intracluster magnetic field in the double relic galaxy cluster Abell 2345. *MNRAS* **502**, 2518–2535 (2021).
23. Johnson, A. R., Rudnick, L., Jones, T. W., Mendygral, P. J. & Dolag, K. Characterizing the Uncertainty in Cluster Magnetic Fields Derived from Rotation Measures. *ApJ* **888**, 101 (2020).
24. Brüggén, M., Bykov, A., Ryu, D. & Röttgering, H. Magnetic Fields, Relativistic Particles, and Shock Waves in Cluster Outskirts. *Space Sci. Rev.* **166**, 187–213 (2012).
25. Stuardi, C. *et al.* Particle re-acceleration and Faraday-complex structures in the RXC J1314.4-2515 galaxy cluster. *MNRAS* **489**, 3905–3926 (2019).
26. Burn, B. J. On the depolarization of discrete radio sources by Faraday dispersion. *MNRAS* **133**, 67 (1966).
27. Sokoloff, D. D. *et al.* Depolarization and Faraday effects in galaxies. *MNRAS* **299**, 189–206 (1998).
28. Govoni, F. *et al.* Polarization of cluster radio halos with upcoming radio interferometers. *Astron. & Astrophys.* **554**, A102 (2013).
29. Loi, F. *et al.* Rotation measure synthesis applied to synthetic SKA images of galaxy clusters. *MNRAS* **490**, 4841–4857 (2019).
30. Lazarian, A., Yuen, K. H., Lee, H. & Cho, J. Synchrotron Intensity Gradients as Tracers of Interstellar Magnetic Fields. *ApJ* **842**, 30 (2017).
31. Lazarian, A. & Yuen, K. H. Gradients of Synchrotron Polarization: Tracing 3D Distribution of Magnetic Fields. *ApJ* **865**, 59 (2018).
32. Hu, Y., Lazarian, A., Li, Y., Zhuravleva, I. & Gendron-Marsolais, M.-L. Probing Magnetic Field Morphology in Galaxy Clusters with the Gradient Technique. *ApJ* **901**, 162 (2020).
33. Goldreich, P. & Sridhar, S. Toward a Theory of Interstellar Turbulence. II. Strong Alfvénic Turbulence. *ApJ* **438**, 763 (1995).
34. Lazarian, A. & Vishniac, E. T. Reconnection in a Weakly Stochastic Field. *ApJ* **517**, 700–718 (1999).
35. Cho, J. & Vishniac, E. T. The Anisotropy of Magnetohydrodynamic Alfvénic Turbulence. *ApJ* **539**, 273–282 (2000).
36. Cho, J. & Lazarian, A. Compressible magnetohydrodynamic turbulence: mode coupling, scaling relations, anisotropy, viscosity-damped regime and astrophysical implications. *MNRAS* **345**, 325–339 (2003).
37. Maron, J. & Goldreich, P. Simulations of Incompressible Magnetohydrodynamic Turbulence. *ApJ* **554**, 1175–1196 (2001).
38. Hu, Y., Xu, S. & Lazarian, A. Anisotropies in Compressible MHD Turbulence: Probing Magnetic Fields and Measuring Magnetization. *ApJ* **911**, 37 (2021).
39. Wang, X., Tu, C., Marsch, E., He, J. & Wang, L. Scale-dependent Normalized Amplitude and Weak Spectral Anisotropy of Magnetic Field Fluctuations in the Solar Wind Turbulence. *ApJ* **816**, 15 (2016).
40. Duan, D. *et al.* Anisotropy of Solar Wind Turbulence in the Inner Heliosphere at Kinetic Scales: PSP Observations. *ApJL* **915**, L8 (2021).
41. Matteini, L. *et al.* Magnetic field turbulence in the solar wind at sub-ion scales: in situ observations and numerical simulations. *Front. Astron. Space Sci.* **7**, 83 (2020).
42. Li, Y. *et al.* Direct Detection of Black Hole-driven Turbulence in the Centers of Galaxy Clusters. *ApJL* **889**, L1 (2020).
43. Brunetti, G. & Lazarian, A. Compressible turbulence in galaxy clusters: physics and stochastic particle re-acceleration. *MNRAS* **378**, 245–275 (2007).
44. Xu, S. & Lazarian, A. Turbulent Dynamo in a Conducting Fluid and a Partially Ionized Gas. *ApJ* **833**, 215 (2016).
45. Knowles, K. *et al.* The MeerKAT Galaxy Cluster Legacy Survey. I. Survey Overview and Highlights. *Astron. & Astrophys.* **657**, A56 (2022).
46. Kale, R., Dwarkanath, K. S., Bagchi, J. & Paul, S. Spectral and polarization study of the double relics in Abell 3376 using the Giant Metrewave Radio Telescope and the Very Large Array. *MNRAS* **426**, 1204–1211 (2012).
47. Lindner, R. R. *et al.* The Radio Relics and Halo of El Gordo, a Massive $z = 0.870$ Cluster Merger. *ApJ* **786**, 49 (2014).

48. Chibueze, J. O. *et al.* Jets from MRC 0600-399 bent by magnetic fields in the cluster Abell 3376. *Nature* **593**, 47–50 (2021).
49. Cho, J., Vishniac, E. T., Beresnyak, A., Lazarian, A. & Ryu, D. Growth of Magnetic Fields Induced by Turbulent Motions. *ApJ* **693**, 1449–1461 (2009).
50. Govoni, F. *et al.* A radio ridge connecting two galaxy clusters in a filament of the cosmic web. *Science* **364**, 981–984 (2019).
51. Botteon, A. The most giant radio structures in the Universe. In *Hypatia Colloquium 2022*, 5 (2022).
52. Cuciti, V. *et al.* Galaxy clusters enveloped by vast volumes of relativistic electrons. *Nature* **609**, 911–914 (2022).
53. Lazarian, A. Enhancement and Suppression of Heat Transfer by MHD Turbulence. *ApJL* **645**, L25–L28 (2006).
54. Willson, M. A. G. Radio observations of the cluster of galaxies in Coma Berenices - the 5C4 survey. *MNRAS* **151**, 1 (1970).
55. Govoni, F. *et al.* Radio and X-ray diffuse emission in six clusters of galaxies. *Astron. & Astrophys.* **376**, 803–819 (2001).
56. Bonafede, A. *et al.* Revealing the magnetic field in a distant galaxy cluster: discovery of the complex radio emission from MACS J0717.5 +3745. *Astron. & Astrophys.* **503**, 707–720 (2009).
57. Churazov, E. *et al.* X-ray surface brightness and gas density fluctuations in the Coma cluster. *MNRAS* **421**, 1123–1135 (2012).
58. Zhuravleva, I. *et al.* Turbulent heating in galaxy clusters brightest in X-rays. *Nature* **515**, 85–87 (2014).
59. Zhuravleva, I., Allen, S. W., Mantz, A. & Werner, N. Gas Perturbations in the Cool Cores of Galaxy Clusters: Effective Equation of State, Velocity Power Spectra, and Turbulent Heating. *ApJ* **865**, 53 (2018).
60. Yuen, K. H. & Lazarian, A. Tracing Interstellar Magnetic Field Using Velocity Gradient Technique: Application to Atomic Hydrogen Data. *ApJL* **837**, L24 (2017).
61. Hu, Y., Lazarian, A. & Stanimirović, S. Revealing Gravitational Collapse in the Serpens G3-G6 Molecular Cloud Using Velocity Gradients. *ApJ* **912**, 2 (2021).
62. Lazarian, A. & Pogosyan, D. Statistical Description of Synchrotron Intensity Fluctuations: Studies of Astrophysical Magnetic Turbulence. *ApJ* **747**, 5 (2012).
63. Brentjens, M. A. & de Bruyn, A. G. Faraday rotation measure synthesis. *Astron. & Astrophys.* **441**, 1217–1228 (2005).
64. Lazarian, A. & Pogosyan, D. Spectrum and Anisotropy of Turbulence from Multi-frequency Measurement of Synchrotron Polarization. *ApJ* **818**, 178 (2016).
65. Urdampilleta, I. *et al.* X-ray study of the double radio relic Abell 3376 with Suzaku. *A@AND@A* **618**, A74 (2018).
66. Duchesne, S. W., Johnston-Hollitt, M. & Bartalucci, I. Low-frequency integrated radio spectra of diffuse, steep-spectrum sources in galaxy clusters: palaeontology with the MWA and ASKAP. *PASA* **38**, e053 (2021).
67. Botteon, A., Gastaldello, F., Brunetti, G. & Kale, R. A $M \gtrsim 3$ shock in ‘El Gordo’ cluster and the origin of the radio relic. *MNRAS* **463**, 1534–1542 (2016).

Acknowledgements

Y.H. and A.L. acknowledge the support of the NASA ATP AAH7546 and NSF grants AST 2307840. K.W.H. acknowledges the support of NASA ATP AAH7546 and the LDRD program of LANL with project # 20220107DR. NASA provided financial support for this work through award 09_0231 issued by the Universities Space Research Association, Inc. (USRA). This work used SDSC Expanse CPU at SDSC through allocations PHY230032, PHY230033, PHY230091, and PHY230105 from the Advanced Cyberinfrastructure Coordination Ecosystem: Services & Support (ACCESS) program, which is supported by National Science Foundation grants #2138259, #2138286, #2138307, #2137603, and #2138296. C.S. and A.B. acknowledge support from the MIUR grant FARE SMS and from the ERC-StG DRANOEL, n. 714245

Author contributions

All authors discussed the results, commented on the manuscript, and contributed to its writing. Y.H. and C.S. analyzed the observational data for radio emission and polarization, while Y.H. and K.W.H. conducted the numerical analysis. Y.H. and A.L. wrote the original manuscript, and A.B. and C.S. provided the observational data. G.B. provided crucial comments and suggestions on the application of SIG to ICM and on physical interpretations of the results.

Competing interests

The authors declare no competing interests.

Synchrotron Intensity Gradient Revealing Magnetic Fields in Galaxy Clusters

Yue Hu^{1,2,*}, C. Stuardi^{3,4}, A. Lazarian^{2,*}, G. Brunetti⁴, A. Bonafede^{3,4}, and Ka Wai Ho^{2,5}

¹Department of Physics, University of Wisconsin-Madison, Madison, WI 53706, USA

²Department of Astronomy, University of Wisconsin-Madison, Madison, WI 53706, USA

³Dipartimento di Fisica e Astronomia, Università di Bologna, via Gobetti 93/2, I-40129 Bologna, Italy

⁴INAF - Istituto di Radioastronomia di Bologna, Via Gobetti 101, I-40129 Bologna, Italy

⁵Theoretical Division, Los Alamos National Laboratory, Los Alamos, NM 87545, USA

*e-mail: yue.hu@wisc.edu, alazarian@facstaff.wisc.edu

Supplementary Information

Low-resolution magnetic field maps in RXC J1314.4 - 2515

Supplementary Fig. 1 displays the low-resolution magnetic field maps in RXC J1314.4 - 2515 determined through SIG and synchrotron polarization. It provides a comparison with the high-resolution SIG measurement in Main Text Fig. 1. The high-resolution SIG measurement in RXC J1314.4 - 2515 (FWHM around 120 kpc) eliminates the resolution difference and shows better agreement with synchrotron polarization compared to the low-resolution measurement (FWHM around 240 kpc).

Uncertainty of the magnetic field direction measured by the SIG

The magnetic field mapped by the SIG method is subject to two sources of uncertainty: (1) systematic errors in the observational map and (2) the uncertainty inherent in the SIG algorithm itself. The latter uncertainty arises from the subregion-fitting approach utilized in the algorithm. Specifically, the SIG fits a Gaussian histogram to the orientation of the gradient within a subregion and outputs the angle corresponding to the peak value of the histogram. The associated uncertainty can be quantified as the error $\sigma_{\psi_s}(x, y)$ of the Gaussian fitting algorithm within a confidence level 95%.

Considering the noise $\sigma_I(x, y)$, which is assumed to be constant, in intensity map $I(x, y)$ and error propagation, the uncertainties $\sigma_q(x, y)$ and $\sigma_u(x, y)$ of the Pseudo Stokes parameters $Q_g(x, y)$ and $U_g(x, y)$ can be obtained from:

$$\sigma_{\cos}(x, y) = |2 \sin(2\psi_s(x, y)) \sigma_{\psi_s}(x, y)|, \quad (1)$$

$$\sigma_{\sin}(x, y) = |2 \cos(2\psi_s(x, y)) \sigma_{\psi_s}(x, y)|, \quad (2)$$

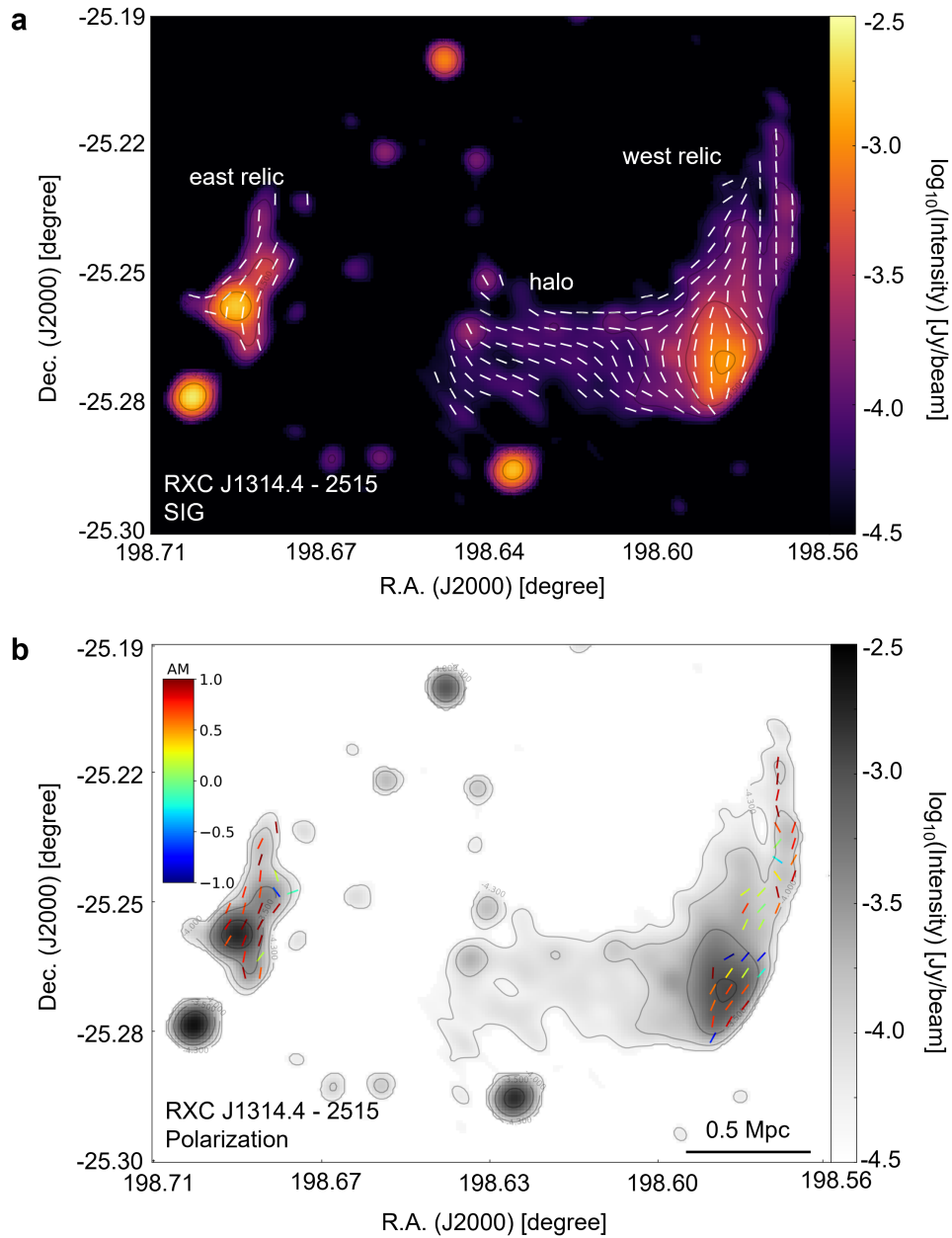
$$\sigma_q(x, y) = |I \cdot \cos(2\psi_s)| \sqrt{\left(\frac{\sigma_I}{I}\right)^2 + \left(\frac{\sigma_{\cos}}{\cos(2\psi_s)}\right)^2}, \quad (3)$$

$$\sigma_u(x, y) = |I \cdot \sin(2\psi_s)| \sqrt{\left(\frac{\sigma_I}{I}\right)^2 + \left(\frac{\sigma_{\sin}}{\sin(2\psi_s)}\right)^2}, \quad (4)$$

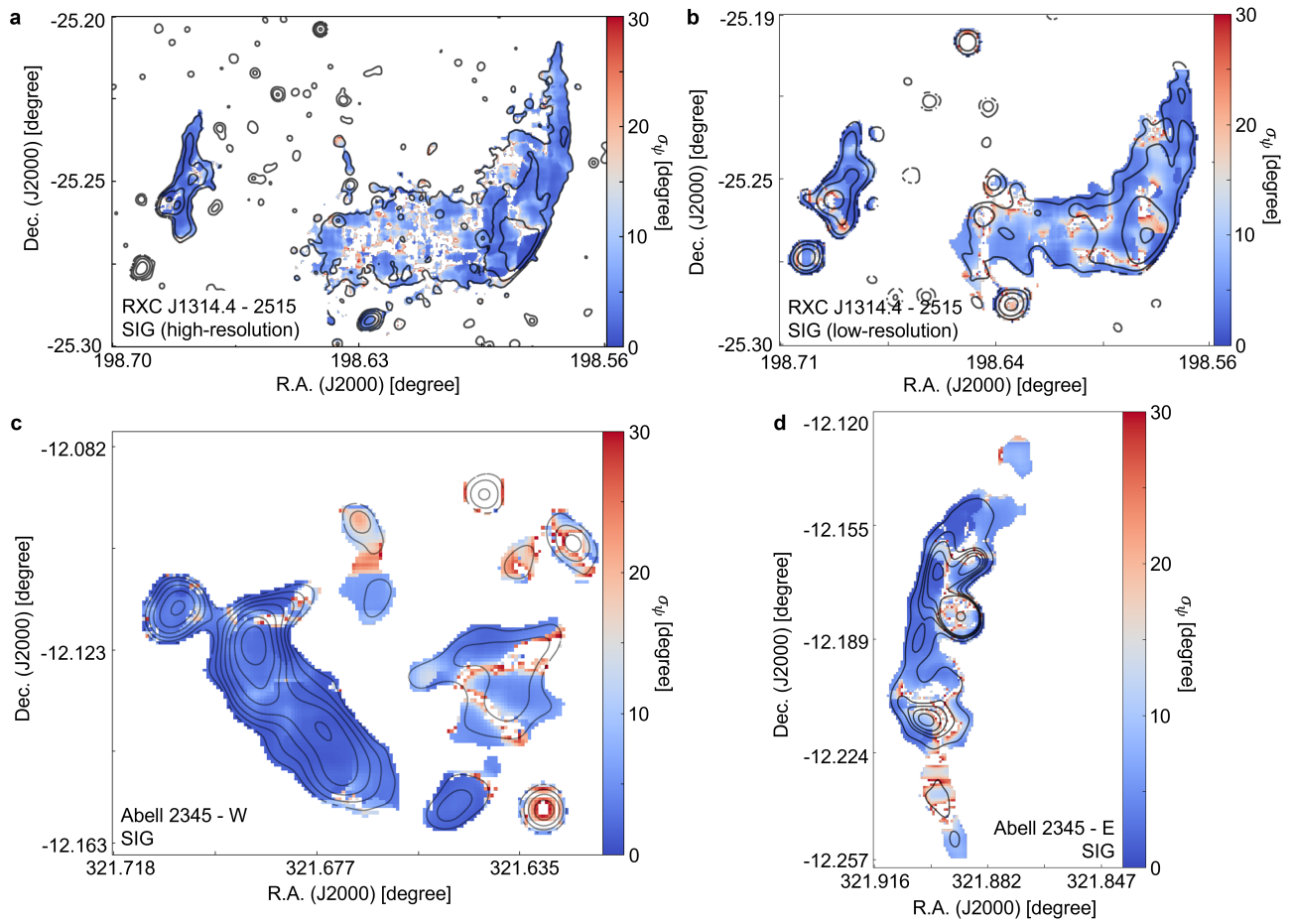
$$\sigma_{\psi_g}(x, y) = \frac{\frac{U_g}{Q_g} \sqrt{\left(\frac{\sigma_q}{Q_g}\right)^2 + \left(\frac{\sigma_u}{U_g}\right)^2}}{2 \left[1 + \left(\frac{U_g}{Q_g}\right)^2\right]}, \quad (5)$$

where $\sigma_{\psi_g}(x, y)$ gives the angular uncertainty of the resulting magnetic field direction. Uncertainty maps are presented in Supplementary Figs. 2 and 3. The median value is listed in Main Text Tab. 2.

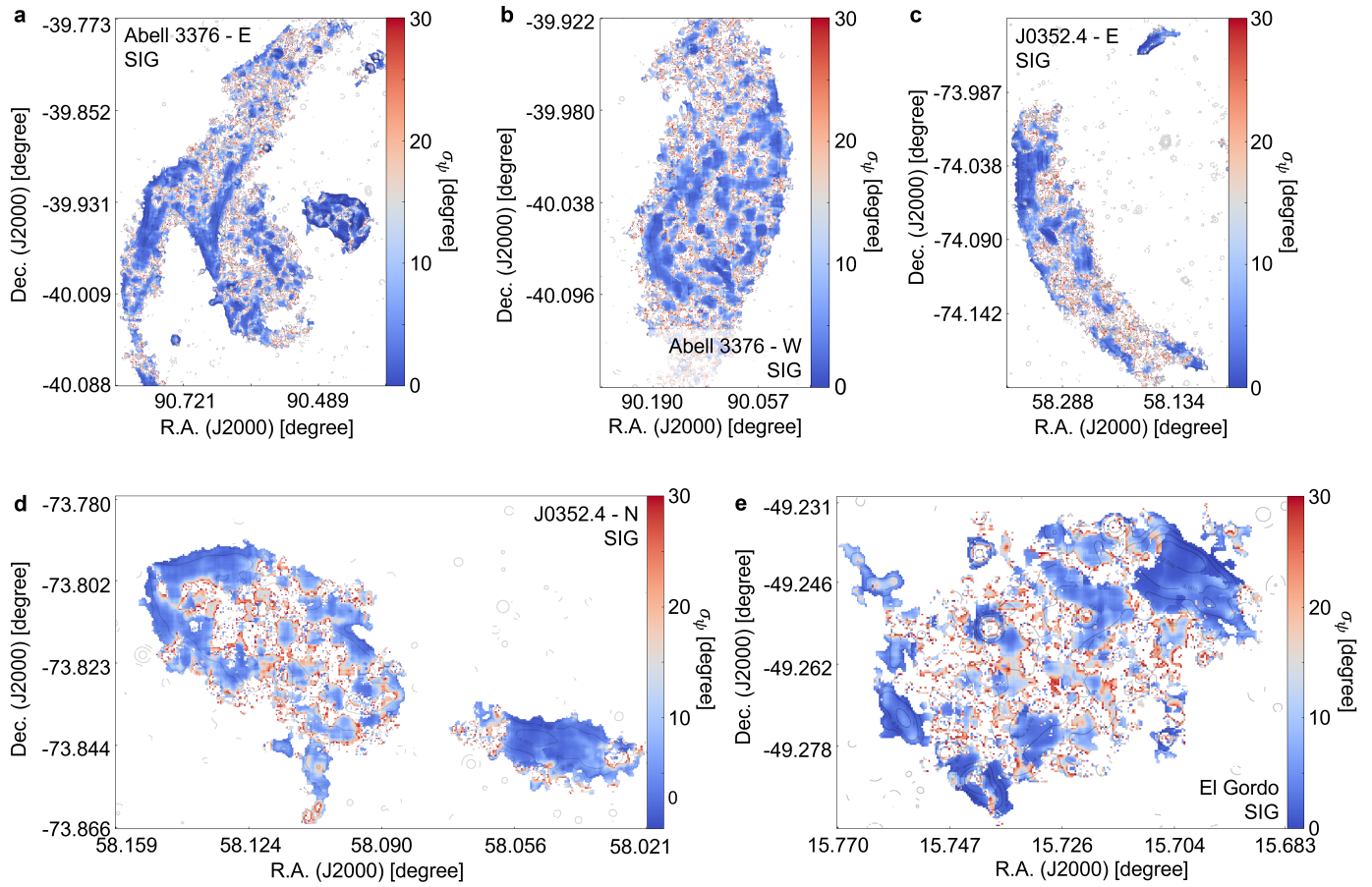
In addition to the signal uncertainty, other physical mechanisms may also have contributed. For instance, the shock front can provide extra gradients, which are not associated with turbulence, but may contribute to the total intensity gradient. In the case of perpendicular shocks, the rapid jump in intensity at the shock front creates an intensity gradient perpendicular to the magnetic field. This relationship between the orientation of the intensity gradient and magnetic field remains true except in the rare case of parallel shock, which is typically not observed in weakly magnetized media¹. However, it is important to note that, in radio relics, SIG is actually measuring the magnetic field at the shock downstream regions, in which the jump of intensity does not appear, so SIG still works there. As for the shock front, it is typically a very thin strip that occupies only one observational beam. The sub-block averaging (over a number of beams) method adopted in SIG, on the other hand, diminishes



Supplementary Figure 1. The magnetic field orientation of the RXC J1314.4 - 2515 cluster. Panel a: the magnetic field mapped by the Synchrotron Intensity Gradient (SIG) technique with an FWHM of approximately 240 kpc. Panel b: the magnetic field determined through synchrotron polarization at 3 GHz using the JVLA radio observations, with an FWHM of approximately 120 kpc. The magnetic field is overlaid on the synchrotron emission intensity map, with colors indicating the AM between the SIG and polarization. Each (magnetic field) segment represents the SIG (or polarization) averaged for 6×6 pixels for visualization purposes. Source data are provided as a Source Data file.



Supplementary Figure 2. Uncertainty maps for the magnetic field measured by the SIG for RXC J1314.4 - 2515 and Abell 2345 clusters. Panels a and b: RXC J1314.4 - 2515's uncertainty maps calculated from high-resolution (panel a) and low-resolution (panel b) observations. Panels c and d: Abell 2345's uncertainty maps calculated for Abell 2345 - W (panel c) and Abell 2345 - E (panel d) observations. Source data are provided as a Source Data file.



Supplementary Figure 3. Same as Supplementary Fig. 2, but for the cluster Abell 3376 (panels a and b), MCXC J0352.4 - 7401 (panels c and d), and El Gordo (panel e). Source data are provided as a Source Data file.

35 the contribution from only one beam. Therefore, we expect that the contribution from turbulence or large-scale flows should
36 dominate the gradient signal.

37 **The relative angle between the POS magnetic field and merger-axis**

38 Supplementary Figs. 4 and 5 present the relative angle between the POS magnetic field and the merger axis as a function of
39 distance from the center of the cluster. The relative angle is determined by averaging over linearly spaced radial bins in annuli
40 from the cluster center. A relative angle value of $> 45^\circ$ signifies that the magnetic field is primarily perpendicular to the merger
41 axis, while a value of $< 45^\circ$ indicates that the magnetic field is predominantly parallel to the axis. The central coordinates for
42 the five studied clusters are: [R.A.: 198.617° , Dec.: -25.261°] for RXC J1314.4 - 2515, [R.A.: 321.796° , Dec.: -12.159°] for
43 Abell 2345, [R.A.: 90.354° , Dec.: -39.998°] for Abell 3376, [R.A.: 58.086° , Dec.: -74.001°] for MCXC J0352.4 - 7401,
44 and [R.A.: 15.718° , Dec.: -49.249°] for El Gordo. The merger axis, determined by the cluster center and the midpoint of
45 the most prominent relic's longer axis, has orientations (north through east) of approximately 80° , -70° , 78° , -30° , -50° for
46 RXC J1314.4 - 2515, Abell 2345, Abell 3376, MCXC J0352.4 - 7401, and El Gordo, respectively. To account for potential
47 uncertainties, we repeat the analysis by rotating the merge axis by $\pm 45^\circ$. However, the merger axis can also be different when
48 derived from the X-ray map elongation or the optical analysis of the merging sub-clusters. Here we further analyze the merger
49 axis determined by the X-ray contour's elongation. The (X-ray) merger axis orients (north through east) approximately 90° ,
50 -15° , 78° , -30° , -30° for RXC J1314.4 - 2515, Abell 2345, Abell 3376, MCXC J0352.4 - 7401, and El Gordo, respectively.

51 The results suggest that magnetic fields in the relics are primarily perpendicular to the merger axis. However, in RXC
52 J1314.4 - 2515 and EL Gordo, the magnetic field in the radio halos is preferentially parallel to the axis within a distance of
53 approximately 0.5 Mpc. As a final note, these correlations are obtained for the POS magnetic field and projected merger axis.

54 **The structure function of POS magnetic field orientation**

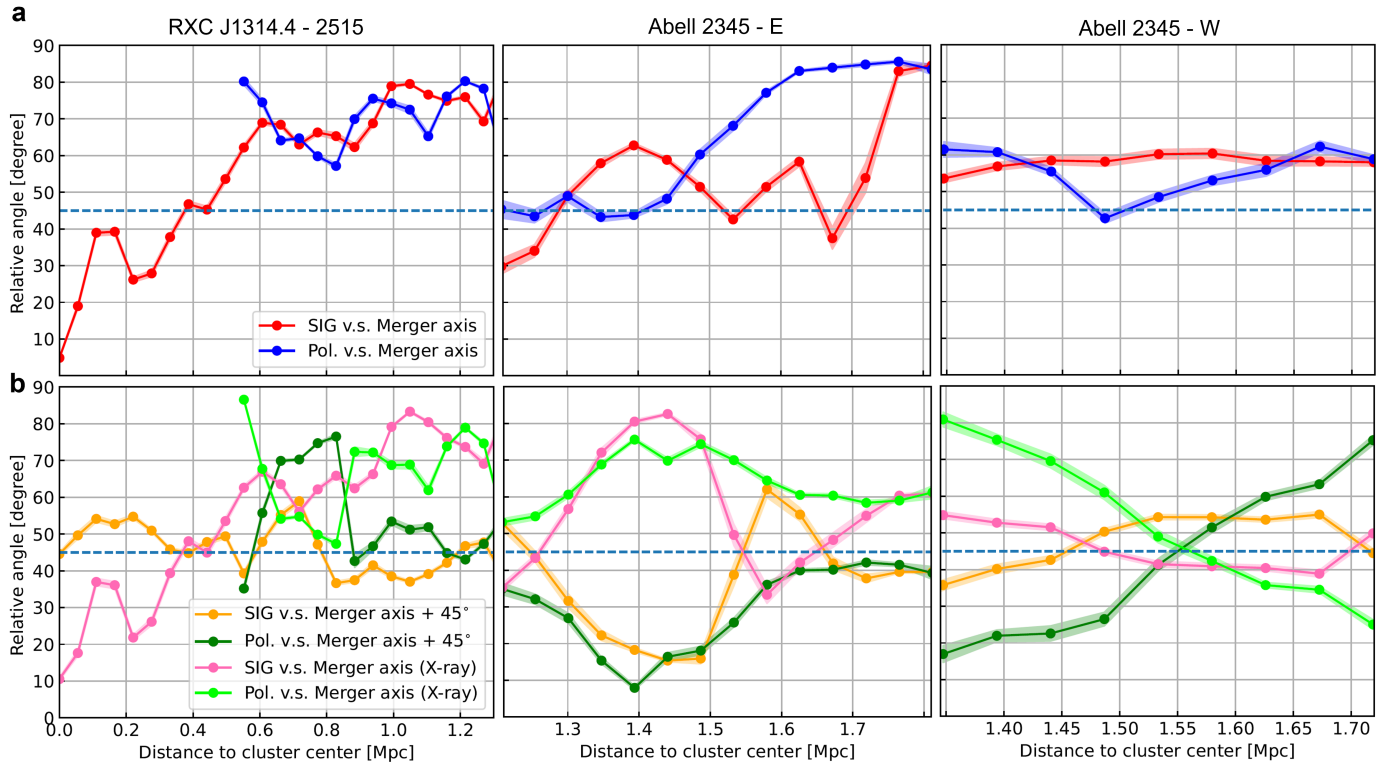
55 Supplementary Fig. 6 presents the structure-function (SF_{θ_r}) of the POS magnetic field orientation in the five clusters RXCJ1314.4
56 - 2515, Abell 2345, MCXC J0352.4 - 7401, Abell 3376, and El Gordo. The structure-function is defined as:

$$SF_{\theta_r}(l) = \langle (\psi(\mathbf{r}) - \psi(\mathbf{r} + \mathbf{l}))^2 \rangle, \quad (6)$$

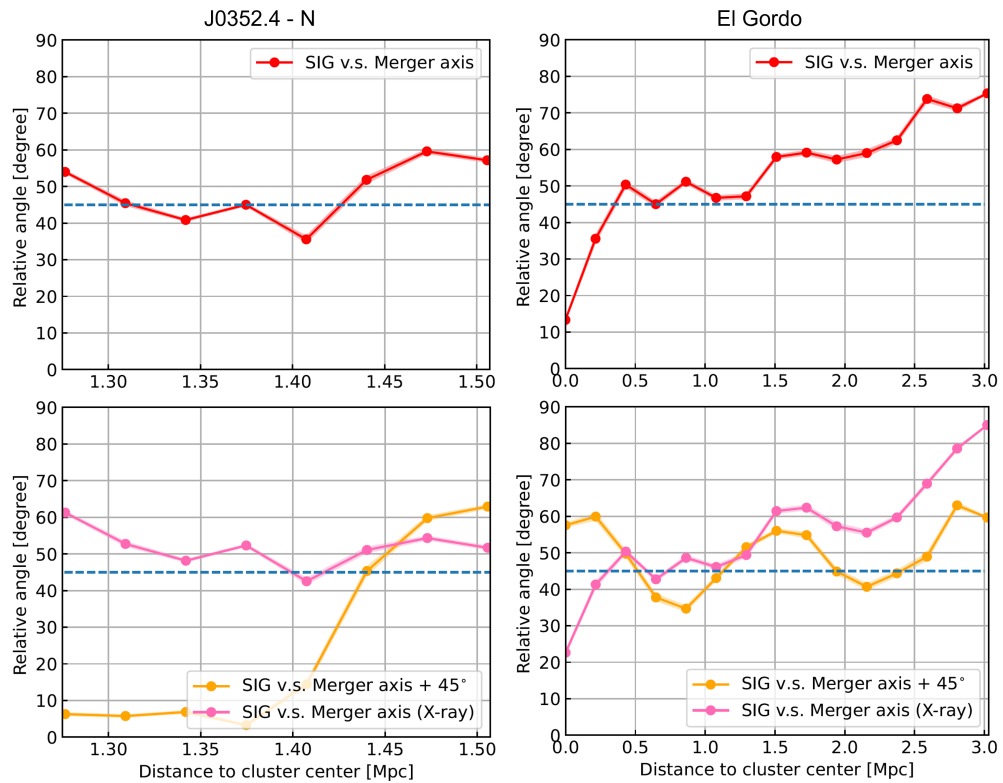
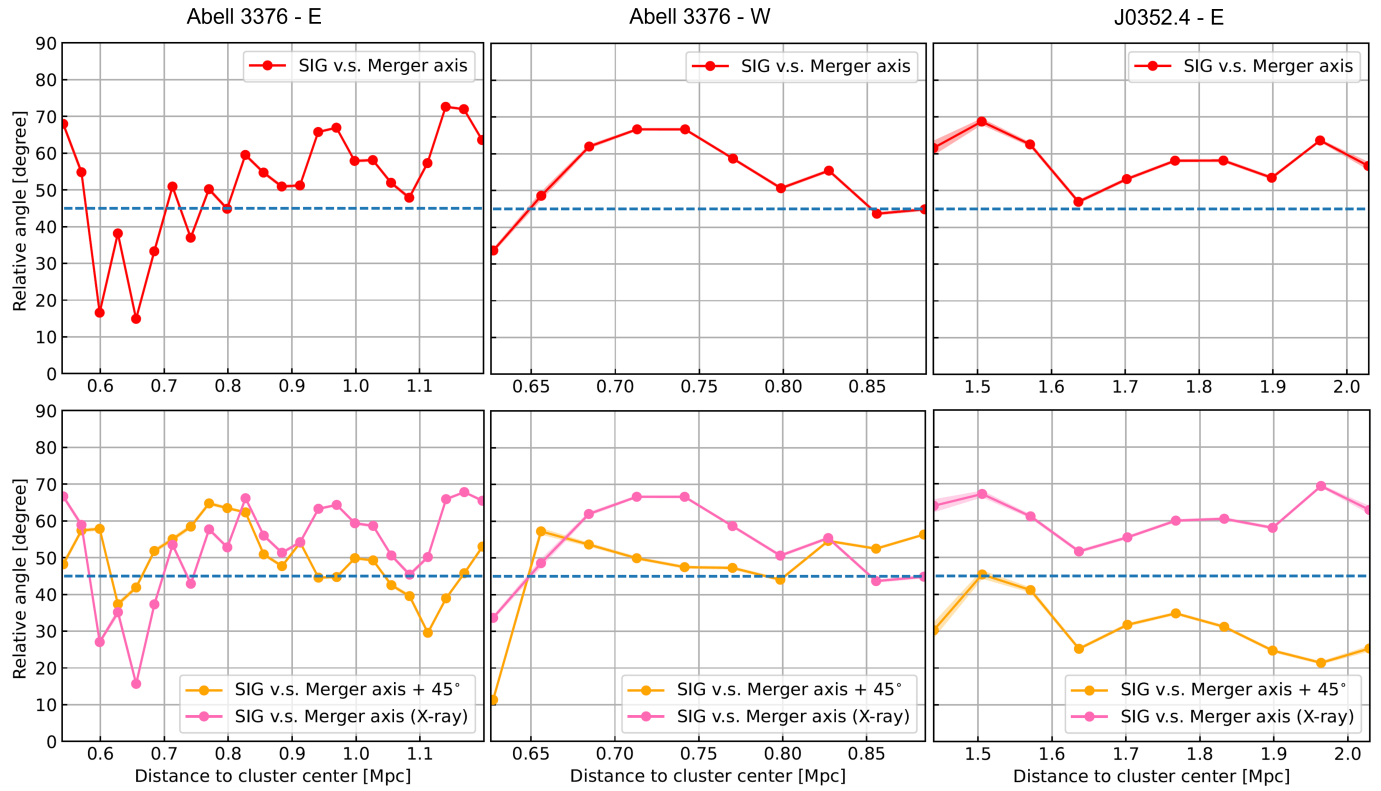
57 where $\psi(\mathbf{r})$ is the magnetic field orientation and $\mathbf{r} = (x, y)$ is the spatial position on the POS. We can see that, for Abell
58 2345, the structure functions of SIG and polarization are flat at large scales and the statistics of SIG are similar to those of
59 polarization. For RXCJ1314.4 - 2515, polarization exhibits more significant angle fluctuations than SIG in the relics (scales
60 larger than > 0.3 Mpc). The difference primarily comes from the less ordered magnetic fields (inferred from polarization)
61 in the west-relic's north tail. The fluctuation of the magnetic field in the radio halo increases further. Generally, for the five
62 clusters, the structure functions are flat on scales larger than > 0.3 Mpc.

63 **References**

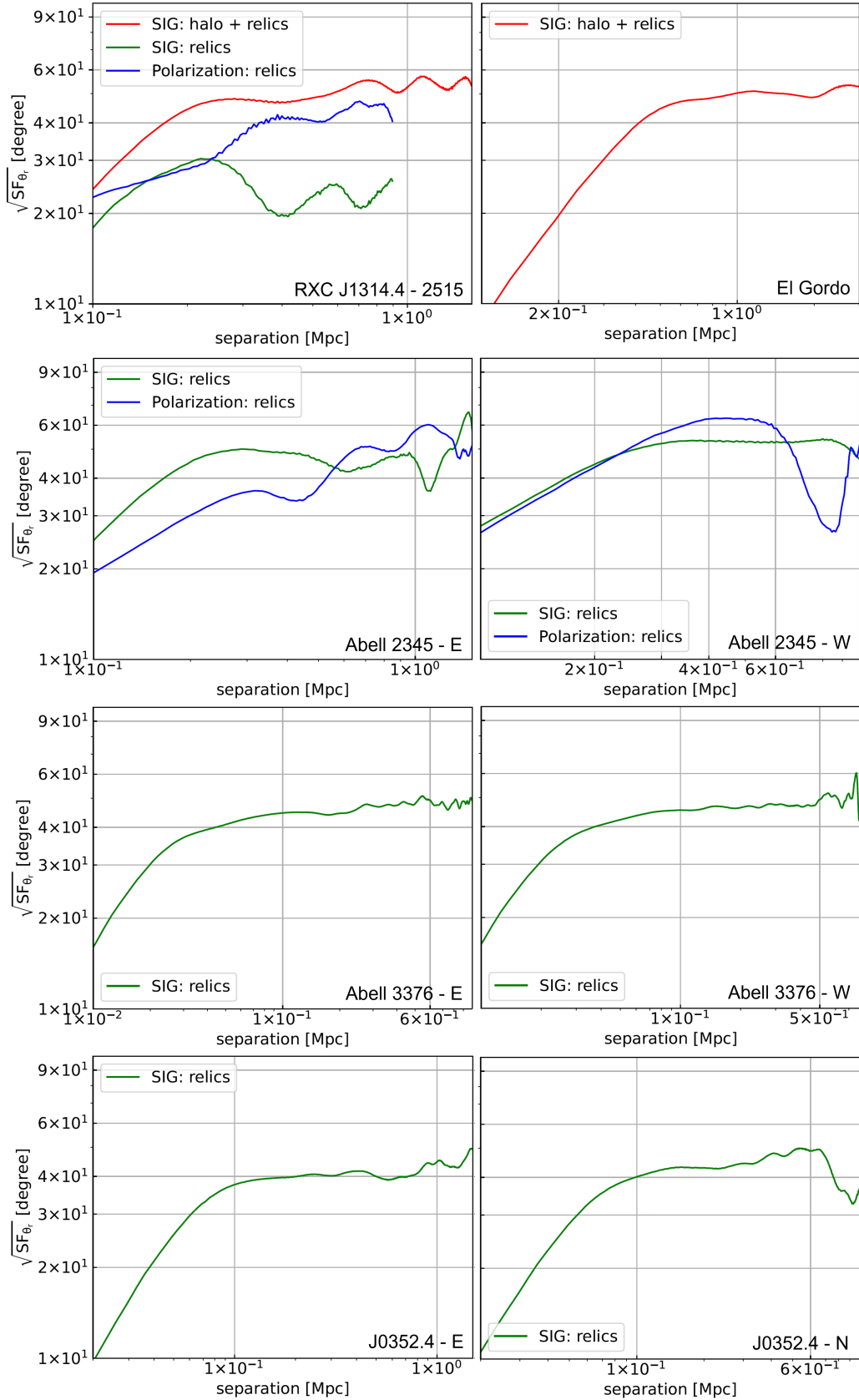
- 64 **1.** Banfi, S., Vazza, F. & Wittor, D. Shock waves in the magnetized cosmic web: the role of obliquity and cosmic ray
65 acceleration. *MNRAS* **496**, 3648–3667 (2020).



Supplementary Figure 4. Panel a: the relative angle between the POS magnetic field and merger-axis (determined by radio observation) as a function of the distance (x -axis) to the cluster center towards the RXCJ1314.4 - 2515 (FWHM approximately 120 kpc) and Abell 2345 (FWHM approximately 180 kpc) galaxy clusters. The relative angle $> 45^\circ$ indicates a preferentially perpendicular configuration, while $< 45^\circ$ suggests a parallel one. The dashed line presents that the relative angle is 45° . The shallower area represents the uncertainty calculated from the standard deviation. Panel b: same as panel a, but the merger axis (derived from radio data) is rotated by $\pm 45^\circ$ or is determined by the X-ray map's elongation. Source data are provided as a Source Data file.



Supplementary Figure 5. Same as Supplementary Fig. 4, but for the clusters MCXC J0352.4 - 7401, Abell 3376, and El Gordo. The dashed line presents that the relative angle is 45° . Source data are provided as a Source Data file.



Supplementary Figure 6. The structure function of the POS magnetic field orientation in five clusters: RXCJ1314.4 - 2515, Abell 2345, MCXC J0352.4 - 7401, Abell 3376, and El Gordo. Source data are provided as a Source Data file.